Tang *et al.*
Chinese Journal of Mechanical Engineering (2023) 36:111
https://doi.org/10.1186/s10033-023-00944-z

Chinese Journal of Mechanical Engineering

ORIGINAL ARTICLE

Open Access

Material Removal Characteristics of Single-Crystal 4H-SiC Based on Varied-Load Nanoscratch Tests

Kun Tang[1*], Wangping Ou[1], Cong Mao[1], Jie Liang[1], Moke Zhang[1], Mingjun Zhang[1] and Yongle Hu[1]

Abstract

Single-crystal silicon carbide (SiC) has been widely applied in the military and civil fields because of its excellent physical and chemical properties. However, as is typical in hard-to-machine materials, the good mechanical properties result in surface defects and subsurface damage during precision or ultraprecision machining. In this study, single- and double-varied-load nanoscratch tests were systematically performed on single-crystal 4H-SiC using a nanoindenter system with a Berkovich indenter. The material removal characteristics and cracks under different planes, indenter directions, normal loading rates, and scratch intervals were analyzed using SEM, FIB, and a 3D profilometer, and the mechanisms of material removal and crack propagation were studied. The results showed that the Si-plane of the single-crystal 4H-SiC and edge forward indenter direction are most suitable for material removal and machining. The normal loading rate had little effect on the scratch depth, but a lower loading rate increased the ductile region and critical depth of transition. Additionally, the crack interaction and fluctuation of the depth-distance curves of the second scratch weakened with an increase in the scratch interval, the status of scratches and chips changed, and the comprehensive effects of the propagation and interaction of the three cracks resulted in material fractures and chip accumulation. The calculated and experimental values of the median crack depth also showed good consistency and relativity. Therefore, this study provides an important reference for the high-efficiency and precision machining of single-crystal SiC to ensure high accuracy and a long service life.

Keywords Single crystal silicon carbides, Varied-load nanoscratch, Material removal, Crack propagation

1 Introduction

As third-generation semiconductor materials with a wide bandgap, single-crystal silicon carbides (SiC), such as 4H-, 6H-, 15R-, and 3C-SiC, are hexagonal, rhombohedral, or cubic structures that have a high hardness, strong stability, low thermal conductivity, favorable temperature resistance, and other excellent physical and chemical properties [1, 2]. Single-crystal SiC is advantageous for producing electronic and sensor devices under extreme temperature, pressure, frequency, power, and radiation conditions and is widely used in the aerospace, telecommunication, automotive, and semiconductor production fields. Recently, researchers have demonstrated increased interest in the performance characterization, applications, and growth of high-quality and large-sized single-crystal SiC [3, 4].

To obtain various high-quality components with low surface damage, grinding, polishing, and other precision and ultraprecision machining methods are used to process single-crystal SiC and ensure high surface integrity in the finished components [5–8]. However, single-crystal SiC is a typical hard-to-machine material due to its high hardness, brittleness, and low fracture toughness [9].

*Correspondence:
Kun Tang
tangkun@csust.edu.cn
[1] Hunan Provincial Key Laboratory of Intelligent Manufacturing Technology for High-performance Mechanical Equipment, Changsha University of Science and Technology, Changsha 410114, China

These properties result in surface defects and subsurface damage such as cracks, scratches, chipping, and spalling during the machining process, which seriously affect the accuracy and service life of the components [10]. Therefore, it is important to study the material removal characteristics and ductile removal mechanism of single-crystal SiC to achieve machining with high efficiency and precision, low emissions, and carbon reduction.

The use of the nanoscratch test with a diamond indenter is an effective method for investigating the material removal mechanism, crack propagation, surface deformation, and damage characteristics in machining and has been widely applied in property tests for various types of workpieces and films.

Huang et al. [11] studied the surface and subsurface deformation characteristics during the nanoscratching of cemented carbide and showed that smooth surfaces were produced at loads of less than 3 mN. When large loads were applied, debris, fractures, and crushed particles were generated. Li et al. [12] systematically studied the effect of strain rate on the surface deformation characteristics and surface damage by conducting nanoscratch tests at different scratch speeds on Lu_2O_3 single crystals. The results showed that a higher scratch speed results in a shallower scratch depth and more continuous chips. Marshall et al. [13] studied transverse crack propagation in the contact field of sharp indenters and discussed the prospect of predicting the transverse fracture degree of other ceramics. Huang et al. [14] performed nanoscratch tests on dense bulk alumina ceramic samples with three grain sizes, and the results showed that the plastic deformation ability of ultra-fine-grained alumina ceramic samples increases at the nano-and microscales. Kovalchenko et al. [15] used abrasive particles of different shapes to characterize monocrystalline silicon. The results showed that spherical WC particles induce a uniform cutting pressure and limit the degree of brittle fracture. Moreover, the sharp edges and corners of the particles produce stress concentration areas, leading to cracking and spalling. Wu et al. [16] studied the lattice bending and dislocations, twins, and stacking faults during the process of carving GaAs. The results showed that the residual stress may be the cause of local lattice bending. Wasmer et al. [17] studied the mechanical deformation of GaAs nanoindentation and scratching and found that twins were the main deformation processes during the indentation process, and only slip bands and ideal dislocations were observed during the scratch process. Qiu et al. [18] conducted double-scratch tests on glass ceramics to study the mechanisms of crack propagation and material removal. The results showed that the interaction between adjacent scratches depends on the scratch depth and separation distance. Cai et al. [19] performed a scratching study on AlN ceramics and found that when the double scratch interval was between 0.5 μm and 1 μm, the second scratch merged with the first scratch to form a single scratch, resulting in an increase in the depth of the second scratch.

In this study, varied-load nanoscratch tests were performed on single-crystal 4H-SiC using a nanoindenter system with a Berkovich indenter to investigate the material removal, crack propagation, surface deformation, and damage characteristics of single-crystal SiC in ultraprecision machining. The material removal characteristics under different planes, indenter directions, loading rates, and scratch intervals are discussed, and the nanoscratch groove surface morphology, distribution law of cracks, material deformations and fractures, and cross-sectional characteristics are analyzed using SEM, FIB, and 3D profilometry. Finally, the mechanisms of material removal and crack propagation in single-crystal 4H-SiC are studied. The proposed research provides a guideline for the high-efficiency and precision machining of single-crystal SiC to ensure high accuracy and a long service life.

2 Experimental Method

The workpiece material was 4H-SiC (Hefei Yuanjing Technology Material Co., Ltd., China), where H and 4 denote the hexagonal structure and periodicity of the tetrahedrons along the [0001] c-axis of the crystal, respectively. The differences between the [0001] Si- and [000-1] C-plane of 4H-SiC in nanoscratch tests are discussed herein. Figure 1 shows the microstructure diagram [20]. The surface of the 5×5×0.41 mm workpiece was polished, and the roughness was less than 15 nm. Additionally, the workpiece was fixed to a copper substrate using a special solid adhesive. The size of the substrate was 20 ×10 ×1 mm, and its surface was polished before adhesive bonding. To ensure cleanliness, it was necessary to clean the workpiece before the tests. First, the workpiece was placed in an acetone solution and rinsed twice using an ultrasonic cleaning machine for 10 min. The samples were then cleaned using distilled water for 10 min before being dried in a dust-free environment.

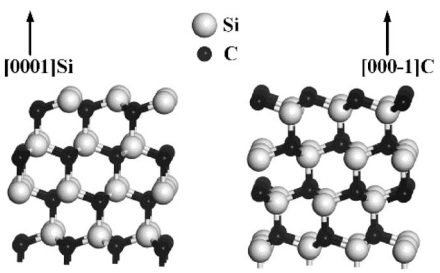

Figure 1 Micro-structure diagram of the Si- and C-plane [20]

As shown in Figure 2, varied-load nanoscratch tests were carried out using a Nano Indenter G200 (Keysight Technologies, USA) to observe the stage and characteristics of the brittle, ductile, and brittle-ductile removal of the materials and to explore the crack propagation and surface deformation of the single-crystal 4H-SiC during machining. The diamond triangular-pyramidal Berkovich indenter was used because it has the same surface and projection area as the Vickers indenter and avoids the influence of the tip cross-edge [21]. The geometric shape of the Berkovich indenter used in this study is shown in Figure 2(b). Its tip radius is 90 nm, the included angle between the centerline and each edge is 77.05°, and the included angle between the centerline and each surface is 65.3° [22].

Figure 3 shows the experimental scheme for the varied-load nanoscratches used in this study. The material removal characteristics under different planes (Si- and C-plane), indenter directions (edge, face, and side face forward), normal loading rate v_p (5, 7, 10 mN/s), and scratch intervals d (3, 5, 8, 11, 14 μm) were discussed, and the mechanism of material removal and crack propagation was also analyzed. A field-emission scanning electron microscope (MIRA3 TESCAN, TESCAN ORSAY HOLDING, a. s., Czech Republic) and a focused ion beam scanning electron microscope (Crossbeam 350, Carl Zeiss Microscopy GmbH, Germany) were employed to observe the microcracks, fractures, and deformations of the surface and subsurface, and an optical surface profilometer was used to determine the 3D morphology and cross-sectional characteristics of the double nanoscratch.

3 Results and Discussions

3.1 Material Removal Characteristics of the Si- and C-plane

Figure 4(a) and (b) show the surface morphology characteristics of the scratches on the Si- and C-planes, respectively. With an increase in loading, the width and depth of the scratches, chips, and both sides of the scratches increased accordingly. Ductile, transition, and brittle regions were distinguished based on groove morphology characteristics to facilitate the comparison of the distinct scratch regions.

In Figure 4(a) and (b), zones (a1)–(a3) and (b1)–(b3) represent some portions and the final part of the scratch, respectively, and diagrams (a4) and (b4) indicate the depth-distance curve of the scratch. No obvious cracks or fractures were observed in either zone (a1) or (b1). However, in zones (a2), (a3), (b2), and (b3), both sides of the scratches began to show the morphological characteristics of some cracks, chunks, and squama-shaped fractures, and this became more evident with the progression of scratching. According to diagrams (a4) and (b4), the scratch groove surface produced the first crack, and the curve began to fluctuate, therefore, the scratch depth at this time was defined as the critical value of the brittle-plastic transition. The critical depths of the ductile-brittle transition [23–25] of the C- and Si-planes on scratching are approximately 212.3 and 105.5 nm, respectively. This shows that the initiation of brittle material removal on the C-plane occurred earlier than that on the Si-plane. Furthermore, in zones (a3) and (b3) of the final part of the scratches, the scratch track of the C-plane deflects and its depth-distance curve exhibits greater fluctuation, whereas the scratch process of the Si-plane is relatively stable. This is possibly related to the element type and mechanical properties of the two planes [26–29] and also indicates that the brittle fracture damage of the C-plane is more serious than that of the Si-plane, where the latter is more suitable for precision or ultra-precision machining.

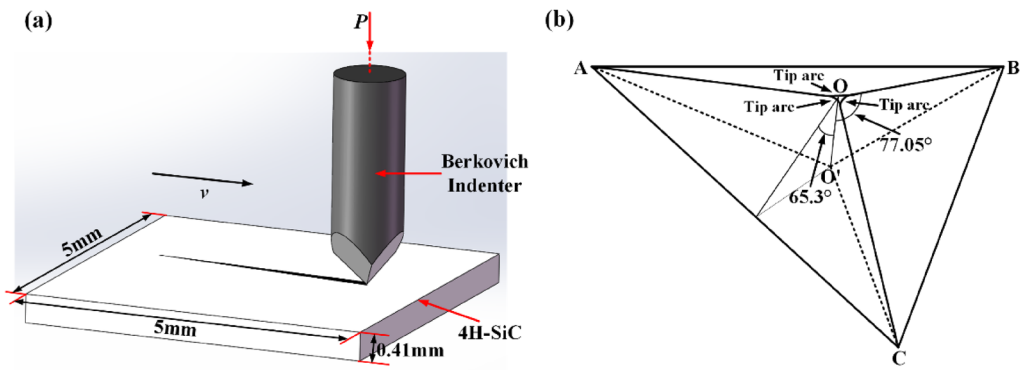

Figure 2 (**a**) Schematic of the nanoscratch process, (**b**) Structural schematic of the Berkovich indenter

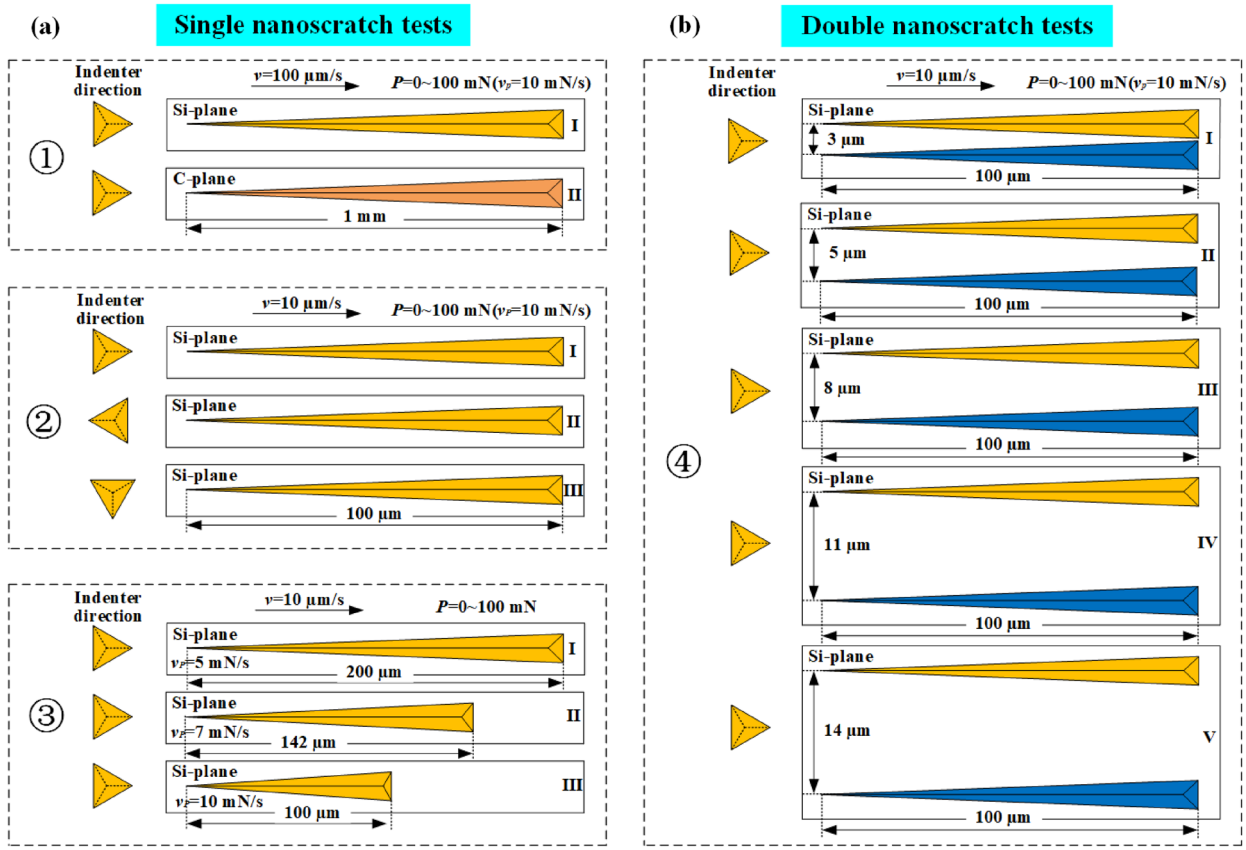

Figure 3 Experimental scheme of (**a**) single and (**b**) double nanoscratch

3.2 Material Removal Characteristics under Different Indenter Directions

Figure 5(a)–(c) show the surface morphology characteristics of the scratch in the indenter directions of the edge, face, and side face forward on the Si-plane, respectively. In Figure 5(a)–(c), zones (a1)–(c1) and (a2)–(c2) represent the middle and final parts of the scratch, respectively, and diagrams (a3)–(c3) indicate the depth-distance curve of the scratch.

In zones (a1)–(c1) and (a2)–(c2), the scratch groove morphology under the indenter direction of the edge forward is smoother and more regular than that of the face and side face forward, and the chips are also fewer in number than those of the last two. Both sides of the scratches exhibited crack and fracture morphological characteristics, and this became more evident as scratching progressed. However, the fractures of the former are mainly squama-shaped, whereas those of the latter two are chunky. According to diagrams (a3)–(c3), the critical depths of the ductile-brittle transition under the three indenter directions are 162.7, 92.1, and 128.1 nm, which correspond to scratch distances of 38.3, 19.2, and 26.1 μm, respectively. This indicates that the initiation for brittle material removal and transition of the first one occur later than those of the last two. This is related to the difference in chip accumulation and stress release under various indenter directions, which is confirmed by the fluctuation range and status of the depth-distance curves. The above images and data indicate that the indenter direction of the edge forward is more suitable for the material removal of single-crystal 4H-SiC compared to the last two, and it also extends the range of the material's ductile region.

3.3 Material Removal Characteristics under Different Normal Loading Rates

Figure 6(a)–(c) show the surface morphology characteristics under normal loading rates of 5, 7, and 10 mN/s, respectively, on the Si-plane. In Figure 6(a)–(c), zones (a1)–(c1) and (a2)–(c2) represent some portions and the final part of the scratch, respectively, and diagrams (a3)–(c3) indicate the depth-distance curve of the scratch.

In zones (a1)–(c1) and (a2)–(c2), both sides of the scratches exhibit crack and fracture morphological characteristics with mainly squama-shaped fractures and significant chip accumulation and fracture generation in the

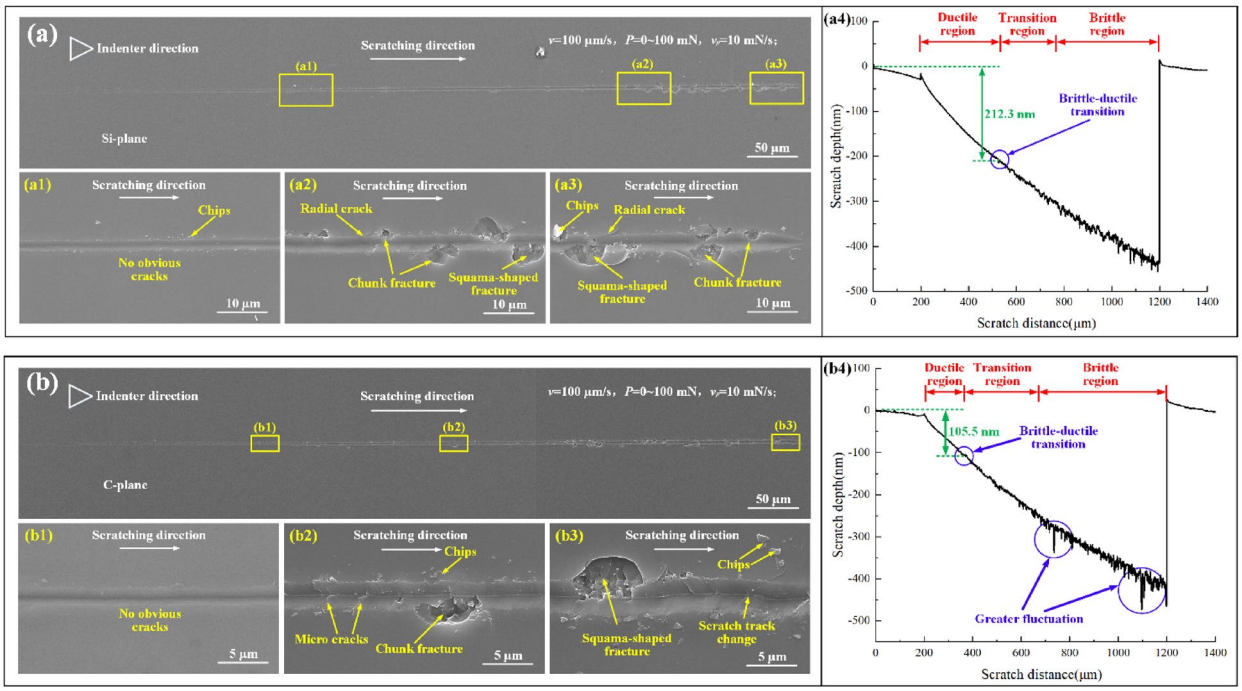

Figure 4 Surface morphology characteristics of scratches: (**a**) Si-plane: (**a1**) Front part, (**a2**) Middle part, (**a3**) Final part, (**a4**) Depth-distance curve; (**b**) C-plane: (**b1**) Front part, (**b2**) Middle part, (**b3**) Final part, (**b4**) Depth-distance curve

final part of the scratches under all three normal loading rates. According to diagrams (a3)–(c3), the critical depths of the ductile-brittle transition under the three rates are 235.2, 186.5, and 154.7 nm, and the scratching depths under a maximum normal load of 100 mN are 418.1, 417.1, and 417.4 nm, respectively. This indicates that the normal loading rate had little effect on the scratch depth under the same maximum normal load. In addition, the ductile region and transition critical depth increase at lower normal loading rates. This can also be reflected by the degree and frequency of the fluctuation of the depth-distance curves.

3.4 Material Removal Characteristics under Different Scratch Intervals

In actual precision and ultraprecision machining such as grinding, lapping, and polishing, multiple scratches that interact with each other are generated on the surfaces of the components. It is necessary to conduct double-varied-load nanoscratch tests to study the effect of the scratch intervals on material removal. Figure 7(a)–(e) show the surface morphology characteristics of the scratch at a scratch interval of 3, 5, 8, 11, 14 μm, respectively, on the Si-plane. As shown in Figure 7, zones (a1)–(e1) and (a2)–(e2) represent some portions and the final part of the scratch, respectively, and diagrams (a3)–(e3) show the depth-distance curve of the scratch. Furthermore, Figure 8 (a)–(e) show the characteristics of a cross-section of the scratch at a distance of 80 μm from the starting point of the scratch. An evident interaction between the materials is observed at this position, and the unloading effect is weaker.

As shown in Figure 7(a) and (b), when the scratch interval is small, the second scratch merges with the first and deflects, and the transverse or radial cracks between the adjacent scratches produce strong interactions, resulting in the removal of a large amount of intermediate material between the two scratches. With an increase in the scratch interval, the crack interaction between the scratches gradually weakens, and only a small number of fractures and chips appear. When the scratch interval is 14 μm, there is no interaction between cracks and scratches, and the material removal is not affected by an adjacent scratch. These characteristics are shown in Figure 7(c). A larger fluctuation is presented in the depth-distance curve of the second scratch and is postponed with an increase in the scratch interval, which also decreases the maximum scratch depth. When the scratch interval exceeds 7 μm, this fluctuation is gradually weakened, and the curves of the two scratches show high coincidence.

Furthermore, as shown in Figure 8, a large quantity of materials accumulates at the end segments of all five groups of double scratches. With the extension of

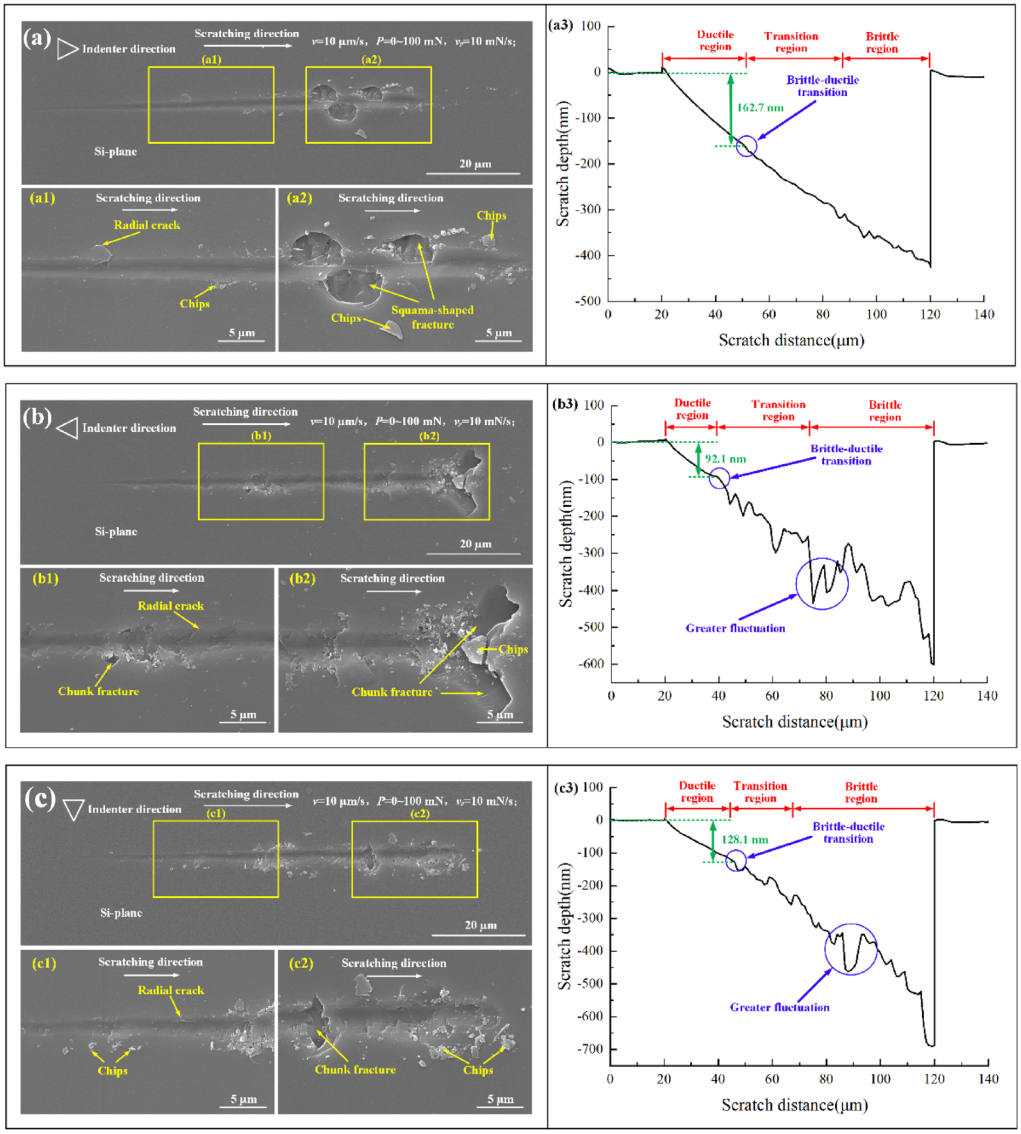

Figure 5 Surface morphology characteristics of scratches under different indenter directions: (**a**) Edge forward: (**a1**) Front part, (**a2**) Final part, (**a3**) Depth-distance curve; (**b**) Face forward: (**b1**) Front part, (**b2**) Final part, (**b3**) Depth-distance curve; (**c**) Side face forward: (**c1**) Front part, (**c2**) Final part, (**c3**) Depth-distance curve

the scratch interval, the status of the double scratches changed from merging and deflecting to separating, and their interaction also decreased. This indicates that it is important to select a suitable abrasive distribution and density to improve the machining accuracy and efficiency of grinding, lapping, and polishing.

3.5 Mechanism of Material Removal and Crack Propagation

For further research on the mechanism and behavior of material removal and crack propagation, the subsurface topography characteristics of single and double scratches on the Si-plane were observed using FIB SEM, as shown in Figures 9 and 10, respectively. As the scratching progressed and the scratch depth increased, radial cracks were generated on the surface, and median and transverse cracks gradually appeared in the subsurface of the workpieces [30]. Moreover, the median and transverse cracks propagated from the subsurface to the surface and interacted with the radial cracks, resulting in the brittle removal of the single-crystal 4H-SiC. This was particularly evident in the middle and final parts of the double scratches, as shown in Figure 10.

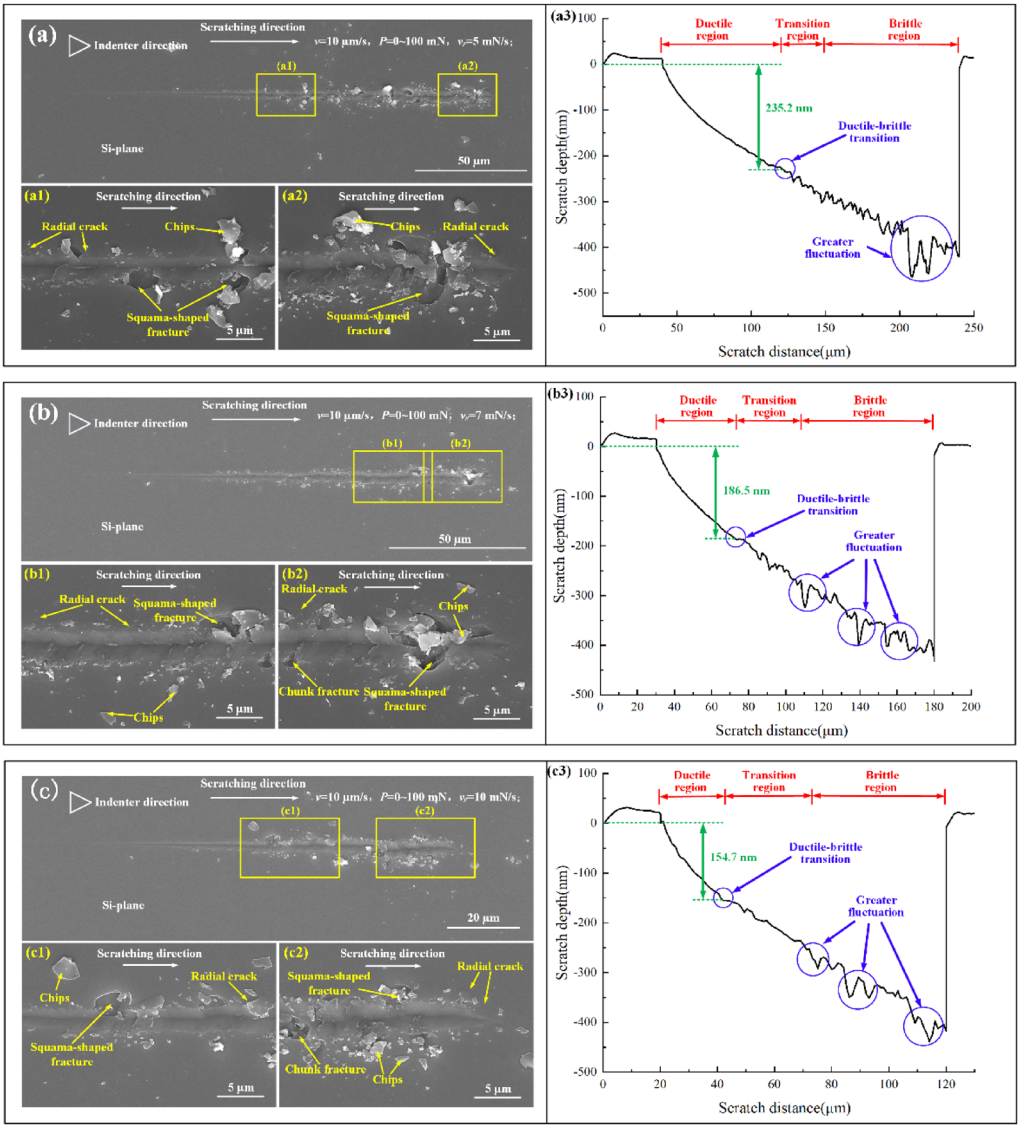

Figure 6 Surface morphology characteristics of scratches under different normal loading rates: (**a**) 5 mN/s: (**a1**) Front part, (**a2**) Final part, (**a3**) Depth-distance curve; (**b**) 7 mN/s: (**b1**) Front part, (**b2**) Final part, (**b3**) Depth-distance curve; (**c**) 10 mN/s: (**c1**) Front part, (**c2**) Final part, (**c3**) Depth-distance curve

In Figures 9(b), 10(c), and (d), squama-shaped fracture can be clearly observed on the surface. Based on research on subsurface cracks in scratches, it was concluded that the squama-shaped fracture was caused by a strong interaction between the transverse crack of the subsurface extending to the material surface and radial crack of the material surface. For a single scratch, the material removal mode is the interaction between the transverse and radial cracks. For double scratches, material removal includes the former as well as the interaction between adjacent scratches.

The progress of material removal and crack propagation can be explained using the models shown in Figures 11 and 12, respectively. Figure 11 shows a schematic of the contact between the indenter and workpiece [31].

For a small load, the tip of the Berkovich indenter can be approximated as a sphere [32], and the scratch hardness can be defined using Eq. (1):

$$H_s = \frac{P}{A_N}, \tag{1}$$

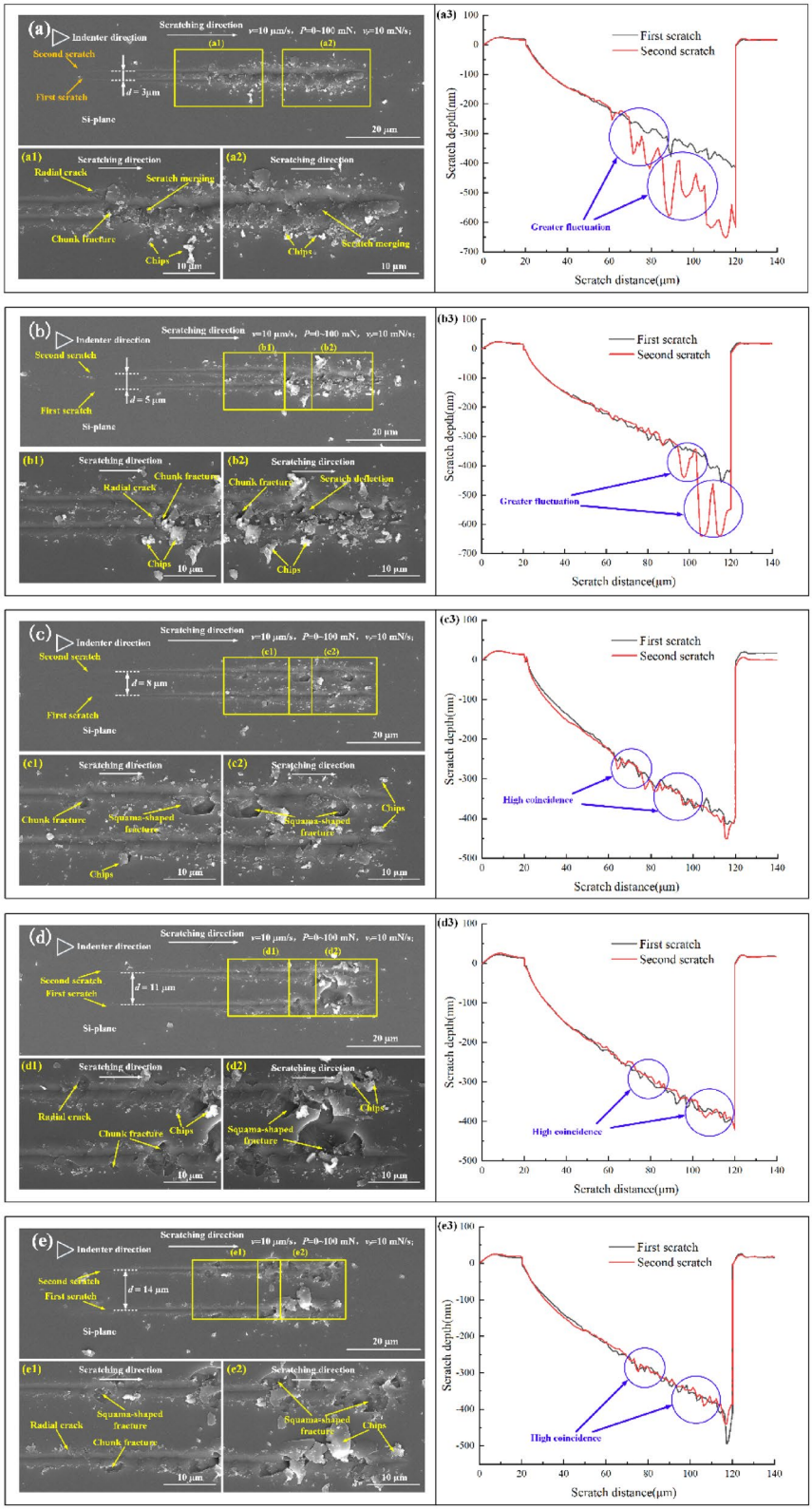

Figure 7 Surface morphology characteristics of the scratches at different scratch intervals: (**a**) 3 μm: (**a1**) Front part, (**a2**) Final part, (**a3**) Depth-distance curve; (**b**) 5 μm: (**b1**) Front part, (**b2**) Final part, (**b3**) Depth-distance curve; (**c**) 8 μm: (**c1**) Front part, (**c2**) Final part, (**c3**) Depth-distance curve; (**d**) 11 μm: (**d1**) Front part, (**d2**) Final part, (**d3**) Depth-distance curve; (**e**) 14 μm: (**e1**) Front part, (**e2**) Final part, (**e3**) Depth-distance curve

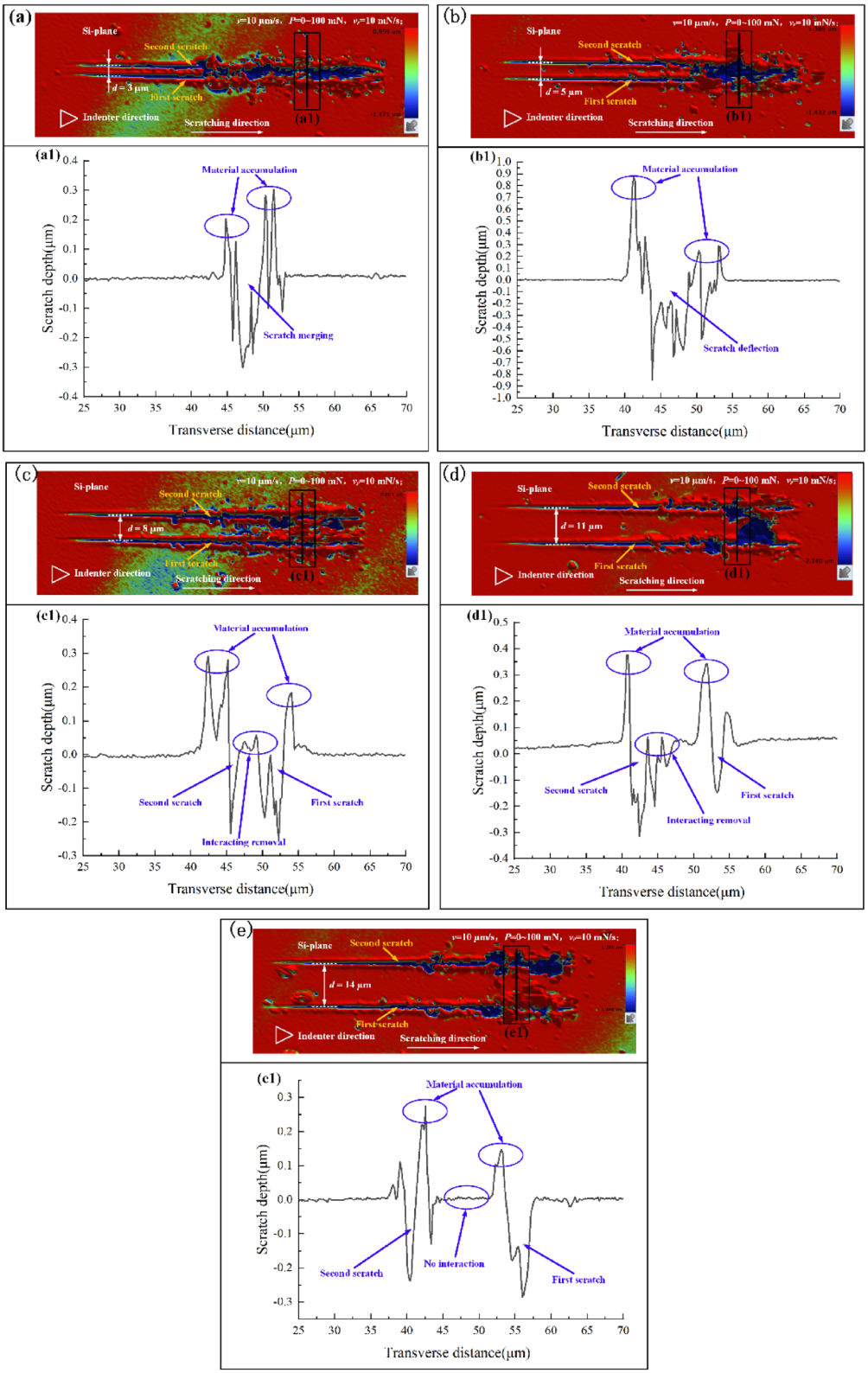

Figure 8 Cross-section characteristics of the scratches under different scratch intervals: (**a**) 3 μm: (**a1**) Profile curve; (**b**) 5 μm: (**b1**) Profile curve; (**c**) 8 μm: (**c1**) Profile curve; (**d**) 11 μm: (**d1**) Profile curve; (**e**) 14 μm: (**e1**) Profile curve

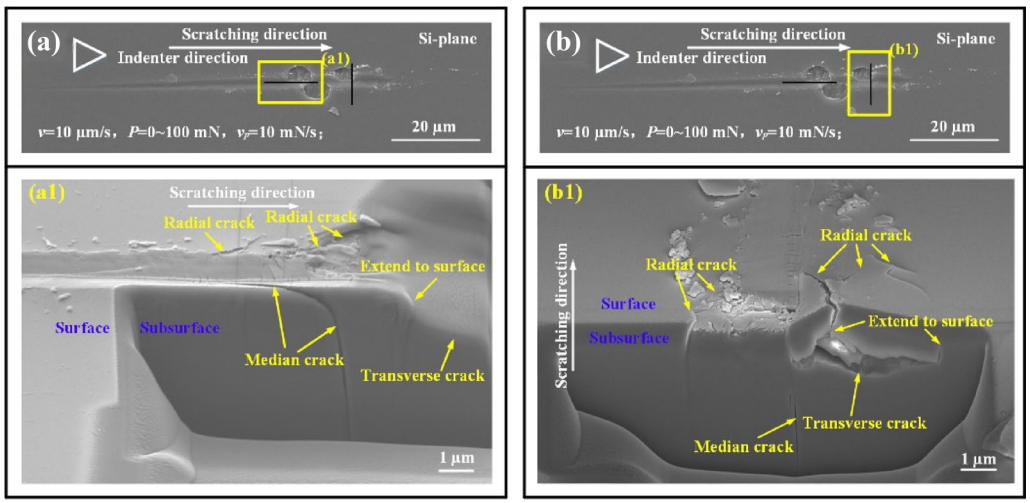

Figure 9 Subsurface topography of the Si face with an indenter edge face forward: (**a**) Direction parallel to the scratch: (**a1**) Subsurface topography; (**b**) Direction perpendicular to scratch: (**b1**) Subsurface topography

where H_s is the scratch hardness (GPa), P is the normal load, and A_N is the projected area of the contact region between the indenter and workpiece. A_N can be approximated using Eq. (2):

$$A_N = \frac{\sqrt{3}}{4}\tan^2(\xi)(3h - 2h_f)h, \tag{2}$$

where ξ is the included angle between the centerline and edge, h is the scratch depth, and h_f is the residual depth. The proportionality coefficient k^* is then introduced, letting $h_f = k^* \times h$. Therefore, the scratch hardness can be calculated as

$$H_s = \frac{P}{\frac{\sqrt{3}}{4}\tan^2(\xi)(3h-2h_f)h} = \frac{P}{\frac{\sqrt{3}}{4}\tan^2(\xi)(3-2k^*)h^2}, \tag{3}$$

When the normal load reaches the critical value of P_c, the material begins to undergo a ductile-brittle transition:

$$P_c = \lambda^* K_{IC}\left(\frac{K_{IC}}{H_s}\right)^3, \tag{4}$$

where λ^* is the dimensionless coefficient and K_{IC} is fracture toughness. The critical depth of the brittle-plastic transition h_{p-b} can be deduced from Eq. (3) and Eq. (4):

$$h_{p-b} = \sqrt{\frac{\lambda^*}{\frac{\sqrt{3}}{4}\tan^2(\xi)(3-2k^*)}}\left(\frac{K_{IC}}{H_s}\right)^2. \tag{5}$$

Figure 12(a) and (b) show the schematics of the single and double scratches, respectively. During nanoscratching, the stress concentration leads to median cracks at the bottom of the contact area with an increase in the load, and the residual stress in the rear area of the indenter leads to transverse and radial cracks. With crack propagation and interaction, material fractures and chip accumulation were observed on the workpiece surface. The transverse crack length C_L and depth C_H were calculated using Eq. (6) and Eq. (7), respectively [13]:

$$C_L = C_2\left(\frac{1}{\tan\beta}\right)^{5/12}\left(\frac{E^{3/4}}{HK_{IC}\left(1-\nu^2\right)^{1/2}}\right)^{1/2}{F_N}^{5/8}, \tag{6}$$

$$C_H = C_2\left(\frac{1}{\tan\beta}\right)^{1/3}\frac{E^{1/2}}{H}{F_N}^{1/2}, \tag{7}$$

where C_2 is a dimensionless constant, E is the elastic modulus, H is the hardness, K_{IC} is the fracture toughness, ν is the Poisson's ratio, F_N is the normal force applied to the indenter, and β is the half apical angle of the indenter.

The radial crack length C_R was calculated using Eq. (8) [33]:

$$C_R = 0.12\left(\frac{E}{H}\right)^{1/3}(\cot\beta)^{4/9}\left(\frac{F_N}{K_{IC}}\right)^{2/3}. \tag{8}$$

Additionally, the median crack depth S can be expressed based on Eq. (9), which is as follows [34]:

$$S = \left\{\left[\alpha_k\left(1+\frac{X_e^M}{X_r^M}e\right)(\cot\beta)^{2/3}\left(\frac{E}{H}\right)^{1/2}\right]\frac{F_N}{K_{IC}}\right\}^{2/3}, \tag{9}$$

where α_k is a correction coefficient ($\alpha_k = 0.1336$), e is a lateral load factor ($e = 1.1$), and X_e^M and X_r^M are indentation coefficients of the elastic stress field and plastic stress field ($X_e^M = 0.032$, $X_r^M = 0.026$), respectively.

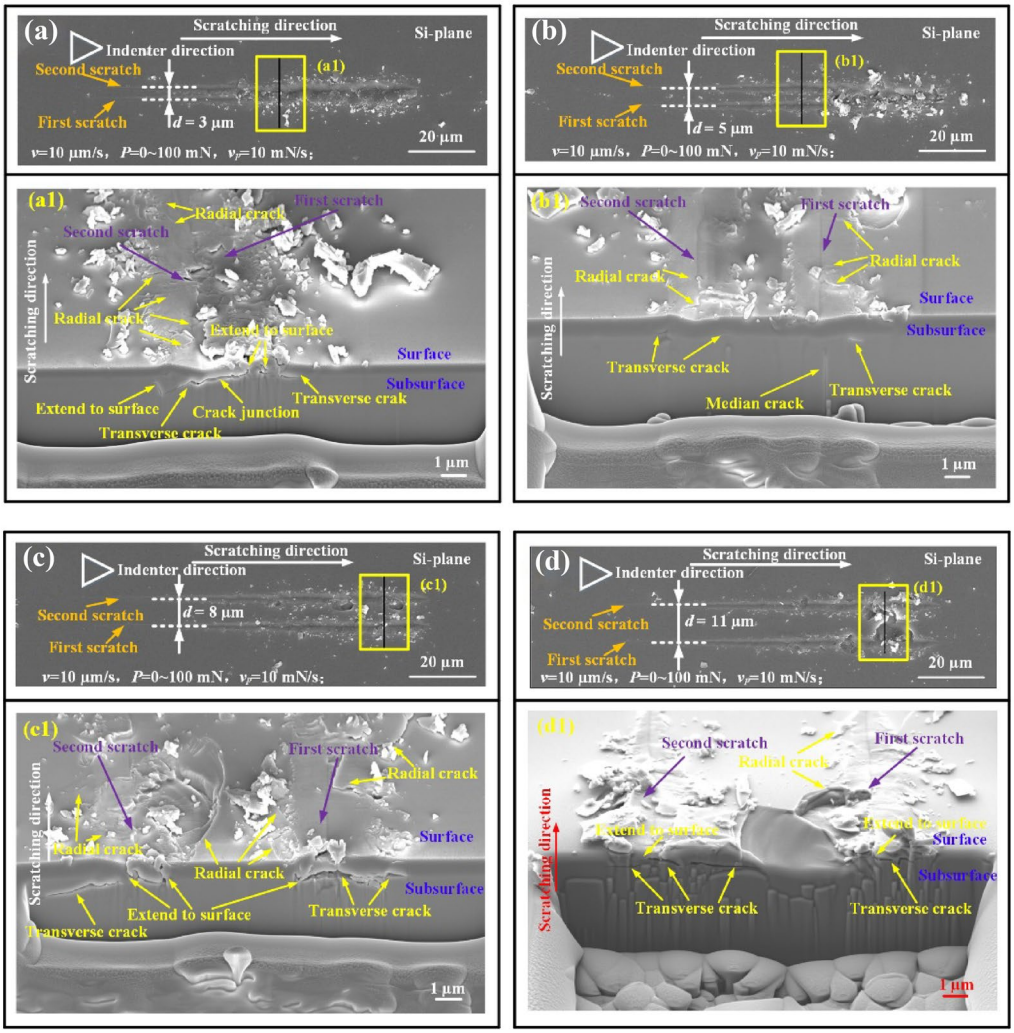

Figure 10 Subsurface topography of the double scratches at different scratch intervals: (**a**) 3 μm: (**a1**) Subsurface topography; (**b**) 5 μm: (**b1**) Subsurface topography; (**c**) 8 μm: (**c1**) Subsurface topography; and (**d**) 11 μm: (**d1**) Subsurface topography

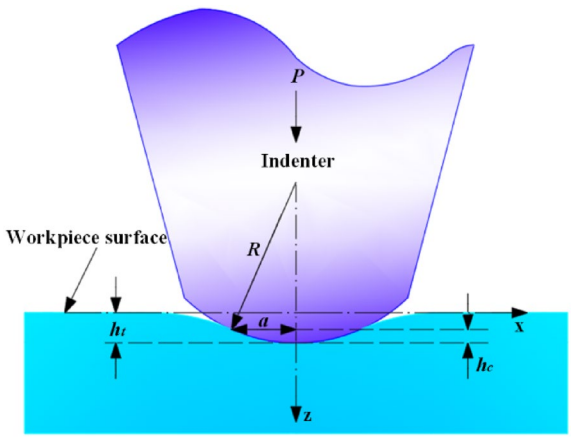

Figure 11 Diagram of the contact region between the indenter and workpiece

The median crack depth, *S*, can be approximated from the edge damage size of the scratch [35]. The edge damage sizes at 10 characteristic positions were measured in the experiments. Figure 13(a) shows the measured values of the edge damage size under normal forces of 67 and 79 mN, whereas Figure 13(b) shows the calculated value of the median crack depth *S* and the experimental data of the edge damage size. The calculated values were fitted using Eq. (9). As shown in Figure 13, the calculated values and experimental data exhibit good consistency and relativity, and the errors between them are less than 10%.

4 Conclusions

In this study, single- and double-varied-load nanoscratch tests were performed on single-crystal 4H-SiC using Berkovich indenter. The main conclusions drawn are as follows:

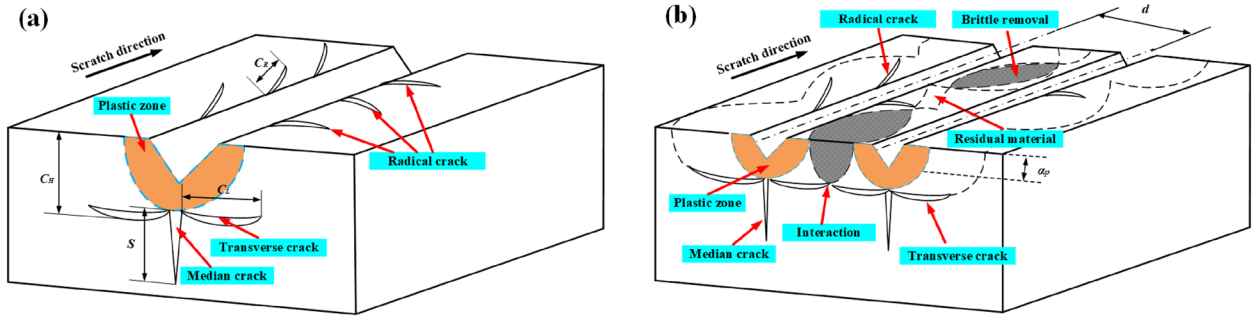

Figure 12 Schematics of the (**a**) single and (**b**) double nanoscratches

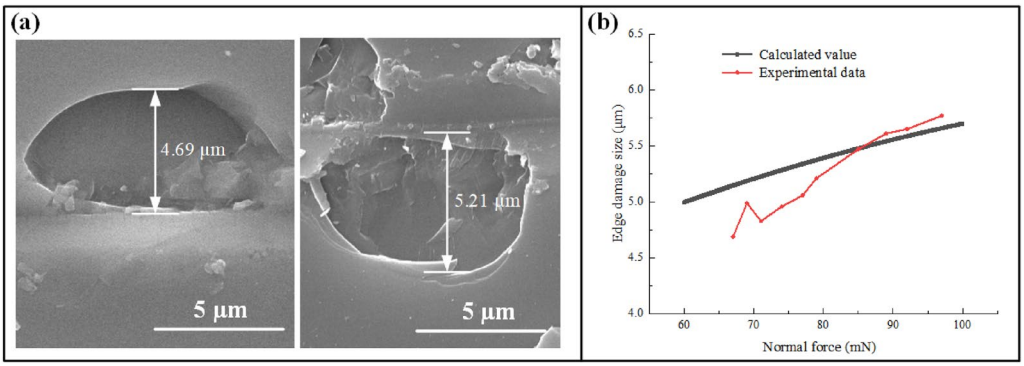

Figure 13 (**a**) Edge damage size at 67 and 79 mN, (**b**) Comparison of the predicted and experimental data

(1) The initiation of brittle removal on the Si-plane occurs later than that on the C-plane, and the scratch process is relatively more stable, making it more suitable for precision or ultraprecision machining.
(2) The scratch groove morphology under the edge forward direction is smoother and more regular than that of the face and side face forward directions, and its brittle removal occurs later than that of the other two. Therefore, the forward direction of the edge is more suitable for the material removal of single-crystal 4H-SiC.
(3) The normal loading rate has little effect on the scratch depth under the same maximum normal load, however, a lower rate increases the ductile region and critical depth of transition.
(4) In the double nanoscratch tests, the crack interaction between the scratches and fluctuation of the depth-distance curves of the second scratch weakens with an increase in the scratch interval, and the status of the scratches and chips also changes. Therefore, it is important to select a suitable abrasive distribution and density to improve machining accuracy and efficiency.
(5) As scratching proceeds, radial cracks are generated on the surface, and median and transverse cracks appear on the subsurface. The propagation and interaction of the three types of cracks result in material fractures and chip accumulation. Moreover, the calculated and experimental values of the median crack depth S exhibit good consistency and relativity.

Acknowledgements
The authors sincerely thank Professors Shao-Hui Yin and Zhi-Xiong Zhou of *Hunan University* for their critical discussions and readings during manuscript preparation.

Authors' Contributions
KT was in charge of the entire trial; WO and KT wrote the manuscript; and JL assisted with sampling and laboratory analyses. All authors read and approved the final manuscript.

Authors' Information
Kun Tang born in 1980, is currently an associate professor at *Hunan Provincial Key Laboratory of Intelligent Manufacturing Technology for High-performance Mechanical Equipment, Changsha University of Science and Technology, China*. He received his Ph.D. degree from *Hunan University, China*, in 2013. His research interests include ultraprecision machining technology, equipment, and intelligent manufacturing.

Wangping Ou born in 1998, is currently a master candidate at *Hunan Provincial Key Laboratory of Intelligent Manufacturing Technology for High-performance Mechanical Equipment, Changsha University of Science and Technology, China*.
Cong Mao born in 1975, is currently a professor at *Hunan Provincial Key Laboratory of Intelligent Manufacturing Technology for High-performance Mechanical Equipment, Changsha University of Science and Technology, China*. He received his Ph.D. degree from *Hunan University, China*, in 2008. His research interests include ultraprecision machining technology, equipment, and intelligent manufacturing.
Jie Liang born in 1995, is currently a master candidate at *Hunan Provincial Key Laboratory of Intelligent Manufacturing Technology for High-performance Mechanical Equipment, Changsha University of Science and Technology, China*.
Moke Zhang born in 1999, is currently a master candidate at *Hunan Provincial Key Laboratory of Intelligent Manufacturing Technology for High-performance Mechanical Equipment, Changsha University of Science and Technology, China*.
Mingjun Zhang born in 1985, is currently an associate professor at *Hunan Provincial Key Laboratory of Intelligent Manufacturing Technology for High-performance Mechanical Equipment, Changsha University of Science and Technology, China*. He received his Ph.D. degree from *Hunan University, China*, in 2013. His research interests include laser-manufacturing technology and equipment.
Yongle Hu born in 1965, is currently a professor at *Hunan Provincial Key Laboratory of Intelligent Manufacturing Technology for High-performance Mechanical Equipment, Changsha University of Science and Technology, China*. He received his Ph.D. degree from *Zhejiang University, China*, in 2009. His research interests include the nonlinear dynamics of mechanical systems, liquid-solid coupling, damage, and fracture mechanics.

Funding
Supported by National Natural Science Foundation of China (Grant No. 51405034), Changsha Municipal Natural Science Foundation of China (Grant No. kq2202200), and Hunan Provincial High-tech Industry Science and Technology Innovation Leading Program of China (Grant No. 2022GK4027).

Declarations

Competing Interests
The authors declare no competing financial interests.

Received: 2 August 2022 Revised: 30 August 2023 Accepted: 1 September 2023
Published online: 25 September 2023

References

[1] L L Snead, T Nozawa, Y Katoh, et al. Handbook of SiC properties for fuel performance modeling. *Journal of Nuclear Materials*, 2007, 371(1-3): 329-377.
[2] L Yin, E Y Vancoille, K Ramesh, et al. Surface characterization of 6H-SiC (0001) substrates in indentation and abrasive machining. *International Journal of Machine Tools and Manufacture*, 2004, 44(6): 607-615.
[3] V V Kozlovski, A A Lebedev, M E Levinshtein, et al. Electrical and noise properties of proton irradiated 4H-SiC Schottky diodes. *Journal of Applied Physics*, 2018, 123(2): 024502.
[4] R T Neil, Y C Yu, J Mihee, et al. Thermal and radiation response of 4H–SiC Schottky diodes with direct-write electrical contacts. *Appl. Phys. Lett.*, 2020, 116(25): 252108.
[5] B B Meng, J Zheng, D D Yuan, et al. Machinability improvement of silicon carbide via femtosecond laser surface modification method. *Appl. Phys. A*, 2019, 125(1): 69.
[6] G L Ma, S J Li, X Liu, et al. Combination of plasma electrolytic processing and mechanical polishing for single-crystal 4H-SiC. *Micromachines*, 2021, 12(6): 606.
[7] H Tanaka, S Shimada. Damage-free machining of monocrystalline silicon carbide. *CIRP Annals*, 2013, 62(1): 55-58.
[8] S Goel, X Luo, P Comley, et al. Brittle–ductile transition during diamond turning of single crystal silicon carbide. *International Journal of Machine Tools and Manufacture*, 2013, 65: 15-21.
[9] J Yan, X Gai, H Harada. Subsurface damage of single crystalline silicon carbide in nanoindentation tests. *Journal of Nanoscience and Nanotechnology*, 2010, 10(11): 7808-7811.
[10] N Wang, F Jiang, X Xu, et al. Effects of crystal orientation on the crack propagation of sapphire by sequential indentation testing. *Crystals*, 2017, 8(1): 3.
[11] R Irwan, H Huang. Surface and subsurface deformation characteristics of cemented tungsten carbide under nanoscratching. *International Journal of Surface Science and Engineering*, 2013, 7(2): 122-134.
[12] C Li, F Zhang, Y Wu, et al. Influence of strain rate effect on material removal and deformation mechanism based on ductile nanoscratch tests of Lu2O3 single crystal. *Ceramics International*, 2018, 44(17): 21486-21498.
[13] D B Marshall, B R Lawn, A G Evans. Elastic/plastic indentation damage in ceramics: the lateral crack system. *Journal of the American Ceramic Society*, 1982, 65(11): 561-566.
[14] L Huang, W Yao, A K Mukherjee, et al. Improved mechanical behavior and plastic deformation capability of ultrafine grain alumina ceramics. *Journal of the American Ceramic Society*, 2012, 95(1): 379-385.
[15] A M Kovalchenko, S Goel, I M Zakiev, et al. Suppressing scratch-induced brittle fracture in silicon by geometric design modification of the abrasive grits. *Journal of Materials Research and Technology*, 2019, 8(1): 703-712.
[16] Y Q Wu, H Huang, J Zou. Lattice bending in monocrystalline GaAs induced by nanoscratching. *Materials Letters*, 2012, 80: 187-190.
[17] K Wasmer, M Parlinska-Wojtan, R Gassilloud, et al. Plastic deformation modes of gallium arsenide in nanoindentation and nanoscratching. *Applied Physics Letters*, 2007, 90(3): 031902.
[18] Z Qiu, C Liu, H Wang, et al. Crack propagation and the material removal mechanism of glass–ceramics by the scratch test. *Journal of the Mechanical Behavior of Biomedical Materials*, 2016, 64: 75-85.
[19] L Cai, X Guo, S Gao, et al. Material removal mechanism and deformation characteristics of AlN ceramics under nanoscratching. *Ceramics International*, 2019, 45(16): 20545-20554.
[20] J Borysiuk, J Soltys, R Bozek, et al. Role of structure of C-terminated 4H-SiC(000-1) surface in growth of graphene layers: Transmission electron microscopy and density functional theory studies. *Phys. Rev. B*, 2012, 85(4): 045426.
[21] T Zhang. *Micro/nano mechanics testing technology*. The Science Publishing Company, 2013. (in Chinese)
[22] J Hay. Instrumented indentation testing. *ASM Handbook of Mechanical Testing & Evaluation*, 2000, 30(2): 106-114.
[23] Y Liu, B Li, C Wu, et al. Smoothed particle hydrodynamics simulation and experimental analysis of SiC ceramic grinding mechanism. *Ceramics International*, 2018, 44(11): 12194-12203.
[24] T G Bifano, T A Dow, R O Scattergood. Ductile-regime grinding: A new technology for machining brittle materials. *Journal of Engineering for Industry*, 1991, 113(2): 184-189.
[25] P Chai, S Li, Y Li. Modeling and experiment of the critical depth of cut at the ductile–brittle transition for a 4H-SiC single crystal. *Micromachines*, 2019, 10(6): 382.
[26] E Konstantinova, M J V Bell, V Anjos. Ab initio calculations of some electronic and elastic properties for SiC polytypes. *Intermetallics*, 2008, 16(8): 1040-1042.
[27] K E Prasad, K T Ramesh. Hardness and mechanical anisotropy of hexagonal SiC single crystal polytypes. *Journal of Alloys and Compounds*, 2019, 770: 158-165.
[28] A V Osipov, A S Grashchenko, A N Gorlyak, et al. Investigation of the hardness and young's modulus in thin near-surface layers of silicon carbide from the Si-and C-faces by nanoindentation. *Technical Physics Letters*, 2020, 46(8): 763-766.
[29] H Kitahara, Y Noda, F Yoshida, et al. Mechanical behavior of single crystalline and polycrystalline silicon carbides evaluated by Vickers indentation. *Journal of the Ceramic Society of Japan*, 2001, 109(1271): 602-606.
[30] B R Lawn, M V Swain. Microfracture beneath point indentations in brittle solids. *Journal of Materials Science*, 1975, 10(1): 113-122.

[31] S Basu, A Moseson, M W Barsoum. On the determination of spherical nanoindentation stress–strain curves. *Journal of Materials Research*, 2006, 21(10): 2628-2637.
[32] P Chai, S Li, Y Li, et al. Mechanical behavior investigation of 4H-SiC single crystal at the micro–nano scale. *Micromachines*, 2020, 11(1): 102.
[33] J C Lambropoulos, S D Jacobs, J Ruckman. Material removal mechanisms from grinding to polishing. *Ceram. Trans.*, 1999, 102: 113-128.
[34] L Wang, Y Gao, X Li, et al. Analytical prediction of subsurface microcrack damage depth in diamond wire sawing silicon crystal. *Materials Science in Semiconductor Processing*, 2020, 112(C): 105015.
[35] P Chai, S Li, Y Li, et al. Study on damage of 4H-SiC single crystal through indentation and scratch testing in micro–nano scales. *Applied Sciences*, 2020, 10(17): 5944.